Appendices

Supporting Materials for Chapter 2

Supporting Text

Justification of assumptions

We modeled Hh signaling in the wing disc using a system of nonlinear partial differential equations [Equations (2.1)-(2.5)]. The general form of the equations is similar to previous morphogen models of the wing disc [1,2,3,4,5]. Here we discuss the approximations used in the formulation of our mathematical model.

Disc Geometry. Wing discs in *Drosophila* are approximately flat larval tissues. We assumed that anterior-posterior (AP) patterning of the disc can be modeled as a one-dimensional system. Because Hh crosses into the anterior compartment from all positions along the AP boundary, a one-dimensional domain is a good approximation of the complicated disc geometry [6]. The subdivision of wing discs into compartments is much more than a convenient definition. The posterior compartment is defined by the expression of the selector gene *engrailed* and cell populations from different compartments do not seem to intermix during development [7]. Thus, the concepts of compartments and AP boundary are well defined in the system. The AP axis of a third instar wing discs is about 200 μm (~80 cells) long [8,9]. We assumed that the AP boundary divides this one-dimensional domain into two equal parts (of 100 μm each).

From our images, this seems a fair approximation. We do not expect that any of these approximations of the disc geometry affect the conclusions of this study.

Disc Growth. Cells in third instar wing discs proliferate in a uniform manner, approximately one division every 8 hours [10]. Since the time-scale of cell proliferation is slow compared to morphogen gradient formation [11,12], in our model we assumed that patterning and growth can be decoupled, and discs are assumed to have a fixed size. A study suggests that the Dpp gradient in the wing disc is not affected by disc growth [13]. Since the Hh gradient specifies the source of the Dpp gradient, it is likely that the Hh gradient is also not affected by disc growth. It is unclear when the Hh gradient forms during wing disc development. However, as the range of Hh is relatively short, the results do not depend on a precise size/stage of the discs.

Equations. *hedgehog* is transcriptionally activated in every posterior cell by the selector gene *engrailed* and we assume that Hh is produced and secreted at a constant rate in all cells of the posterior compartment [Equation (2.1)]. Hh transport into the anterior compartment is a complex process and requires heparan-sulfate proteoglycans and lipoproteins [14,15], but it is mainly transported extracellularly and not by sequential rounds of dynamin-dependent endocytosis/exocytosis [16,17]. We assume that this transport process can be modeled as an effective diffusion process [Equation (2.1)]. This seems to be a good approximation [4,6].

Ligand-Receptor binding reaction is modeled as a mass-action law; in this case, the rate of Hh_Ptc formation is proportional to the product of [Hh] and [Ptc] [Equations

(2.1)-(2.3)]. Because upon Hh binding to Ptc, the Hh_Ptc complex is internalized and targeted to degradation [16], we modeled the Hh+Ptc$\rightarrow$ Hh_Ptc reaction as irreversible, i.e., once the Hh_Ptc complex is formed and internalized, the Ptc receptor cannot be reused and the Hh ligand cannot be re-secreted [Equation (2.1)]. This assumption is supported by experimental data [16], but in any case, assuming that the reaction Hh_Ptc$\rightarrow$Hh+Ptc occurs at a slow rate (compared to the inverse reaction) it does not affect the conclusions of this study (data not shown). We modeled the distribution of the receptor Ptc, both mRNA and protein, in space and time. *ptc* is constitutively present at low levels in the anterior compartment, but in addition, it is transcriptionally upregulated by Hh signaling. Hh-dependent *ptc* transcription is modeled using a Hill function that depends on the levels of signaling activity, here represented by the variable [Signal] [Equation (2.1)]. In Equation (2.3), the rate of *ptc* translation is assumed proportional to [*ptc*] as in other studies [18].

A molecular model of how Smo activation depends on Ptc and Hh_Ptc is missing, but a study has reported the ability of Hh-Ptc complexes to titrate the inhibition of Ptc on signal activation [19]. We use these phenomenological observations to model the rate of "Signal" activation as a Hill function of the [Hh_Ptc] to [Ptc] ratio [Equation (2.5)]. Although the choice of this Hill function is not directly justified by chemical reactions, experimental data suggests that the rate of "Signal" activation is a saturation curve that depends on the [Hh_Ptc] to [Ptc] ratio [19] (see also Fig. 2.1D). Numerical simulations suggest that other choices of sigmoid curves do not affect our conclusions (data not shown). We do not include equations for other Hh target genes in Figure 2.1B because their profiles are only outputs of the system and are not required for the analysis.

Initial and Boundary Conditions. The initial conditions of the system are unclear, since many of the genes involved in Hh signaling may be expressed early in wing disc development. Nevertheless, we administered the initial conditions which are demonstrated sufficient to rescue patterning to approximate wild-type conditions when the system is reinitialized artificially using the *hh* temperature sensitive mutation *hh*[ts2] [20]. Since *ptc* is expressed in a Hh-independent way at low levels in the anterior compartment, we set the following initial conditions (I.C.) for [*ptc*] and [Ptc],

(I.C. 1) $\quad [ptc](x,0) = \dfrac{S^+(x)\alpha_{ptc0}}{\beta_{ptc}} = \dfrac{\alpha_{ptc0}}{\beta_{ptc}}$ for $x > 0$, and zero otherwise,

(I.C. 2) $\quad [Ptc](x,0) = \dfrac{T_{Ptc}}{\beta_{Ptc}}[ptc](x,0)$.

All other terms in the mathematical model are set to zero initially. Unlike other theoretical studies [3,6], we have explicitly included the posterior compartment in our model and simulations. This simplifies (and makes irrelevant) the choice of the posterior boundary condition. Also, because the range of the Hh gradient is short compared to the size of the anterior compartment, the results are largely independent of the choice of the anterior boundary condition. In our simulations, we use zero-flux boundary conditions (B.C.) at $x = \pm 100$ μm,

(B.C.) $\qquad \dfrac{\partial[\mathrm{Hh}]}{\partial x}\bigg|_{x=-100} = \dfrac{\partial[\mathrm{Hh}]}{\partial x}\bigg|_{x=100} = 0$.

Parameters

The parameter values used in the computer simulations of Equations (2.1)-(2.5) are reported in Supporting Table 2.1. Parameter values were either extracted from the

literature, or estimated from experimental or empirical measurements. In this section, we discuss the estimation of those parameters that are not extracted explicitly from the literature. Third instar wing disc cells have an approximate diameter of 2.5 μm and an approximate volume of 2×10^{-14} litres [6]. When parameters are reported in other units, we use these factors to convert parameters into units of Molar.

Hh effective diffusion coefficient (D). The Hh diffusion coefficient has not been measured. For Dpp and Wingless in the wing disc, reported values are 0.1 and 0.5 μm^2/s, respectively. Hh transport seems more similar to that of Wingless, which also requires lipoparticles [15]. Therefore, we estimated $D = 0.5$ μm²/s.

Hh production-secretion rate (α_{Hh}). We assumed that extracellular levels of Hh are about 1μM in the posterior compartment; this is similar to the levels of Dpp in the source of the Dpp gradient. Since the maximum levels of Hh, Hh_{Max}, are given by $Hh_{Max} = \dfrac{\alpha_{Hh}}{\beta_{Hh}}$, we have that $\alpha_{Hh} = (1 \ \mu M)\beta_{Hh}$.

Hh-Ptc association rate (γ_{Hh_Ptc}). We use $\gamma_{Hh\_Ptc} = 0.12 \ \mu M^{-1} \ s^{-1}$ as used for analysis of the Dpp system [6].

Hh degradation rate (β_{Hh}). The characteristic space-constant, λ, of an exponential concentration gradient is formally defined as the distance at which the concentration drops by a factor of 1/e of its maximal intensity. For a morphogen gradient established by diffusion (D) and linear degradation (β), we have $\lambda^2 = \dfrac{D}{\beta}$. However, if in addition, Hh is degraded by binding its receptor, we have that the space constant is

$$\lambda_{Hh} \approx \sqrt{\frac{D}{\beta_{Hh} + \gamma_{Hh\_Ptc} <Ptc>}}$$ where <Ptc> is the average unoccupied Ptc receptors in the

Hh operating domain. Based on computer simulations, we estimated an average of 65% unoccupied Ptc. Studies have reported $\lambda_{Hh} \approx 3.5$ μm [21], which permits the following

estimation, $\beta_{Hh} \approx \frac{D_{Hh}}{\lambda_{Hh}^2} - \gamma_{Hh} <Ptc> = 3.4 \times 10^{-3}$ s^{-1}.

ptc translation rate (T_{Ptc}). The control of mRNA translation is precisely regulated in different eukaryotic cells. For example, the rate of rabbit globin translation when globin mRNA is injected into Xenopus oocytes is 110 globin proteins per mRNA molecule per hour [22], and this number does not appear to change in different embryonic stages or cell types [23]. Since rabbit globin mRNA is 650 base pairs (bp) [24], we estimated that the rate of translation in eukaryotes is about 20 bp/sec. Thus, T_{Ptc} is obtained using this estimated rate of translation as well as information that the *ptc* mRNA is 5535 bp in length (www.flybase.org).

Ptc and Hh_Ptc degradation rates *(β_{Ptc} and $\beta_{Hh\ Ptc}$)*. It has been proposed that Ptc internalization and degradation is independent of Hh binding [25]. Therefore, we assume that $\beta_{Ptc} = \beta_{Hh\_Ptc}$. We use the receptor degradation rate measured in other vertebrate receptors which is consistent with the rapid turnover of Ptc when Hh signaling is shut off in hh^{ts2} discs [8].

ptc transcription rate *(α_{ptc} and α_{ptc0})*. In our experiments, Ptc is detected as soon as 2 hours after Hh signal is recovered (Fig. 2.2E) suggesting that [*ptc*] levels can build up within 2 hours. Maximum receptor levels in this system have been estimated at approximately 1,600 per cell [6]; this gives 0.48 μM. Therefore, we can estimate *ptc*

maximum levels as $\dfrac{\alpha_{ptc}}{\beta_{ptc}} = \dfrac{(0.48\ \mu M)\beta_{Ptc}}{T_{Ptc}} = 0.2\ \mu M$. If these levels can be reached within

approximately 2 hours, then the rate of *ptc* activation is $\alpha_{ptc} = \dfrac{0.2\ \mu M}{7200\ s} \approx 2.7 \times 10^{-5} \mu M\ s^{-1}$.

Finally, the Hh-independent levels in the anterior compartment are about 7-fold lower

than in the Hh-induced *ptc* domain [19]. Therefore, we set $\alpha_{ptc0} = \dfrac{\alpha_{ptc}}{7}$.

ptc degradation rate *(β*_{ptc}*)*. From the previous computation, $\beta_{ptc} = \dfrac{\alpha_{ptc}}{0.2\ \mu M} \approx 1.4 \times 10^{-4} s^{-1}$.

"Signal" activation rate *(α*_{Signal}*)*. We assume that signal activity depends on the rates of

Smo phosphorylation. The maximum levels of pSmo are assumed to be 0.3 μM. Denef et

al. [26] showed that a pSmo replaces unphosphorylated Smo within 30 minutes after

exposure   to   Hh   in   cell   culture   [26].   Therefore,   we   estimate

$\alpha_{Signal} = \dfrac{0.3\ \mu M}{1800\ s} \approx 1.7 \times 10^{-4} \mu M\ s^{-1}$.

"Signal"   degradation   rate   *(β*_{Signal}*)*.   From   the   last   expression,   we   obtain,

$\beta_{Signal} = \dfrac{\alpha_{Signal}}{0.3 \mu M} \approx 5.5 \times 10^{-4}\ s^{-1}$.

[Signal] level required for *ptc* half-maximal activation *(k*_{ptc}*)*. We simulated the system

and found a value of k_{ptc} to support a *ptc* domain which is 5 cells wide.

Hh_Ptc:Ptc ratio required for half-maximal activation of Signal *(k*_{Signal}*)*. Casali and Struhl

suggested that this ratio is approximately two [19].

Hill coefficients (m and n). We set m=3 [2]. In the text (see also discussion below), we

estimated n > 6.8, (n > 4.0 in the more stringent scenario). In all the simulations, however

(except for Figure 2.1C), n was set to 6.8.

Steady-State analysis

At the steady state, it is possible to reduce the full model [Equations (2.1-2.5)] to a single equation of [Hh]. Setting the right-hand side of Equations (2.1-2.5) to zero, and making the necessary algebraic substitutions we obtain the following boundary-value problem

$$D\frac{d^2[\mathrm{Hh}]_{\mathrm{ss}}}{dx^2} + S^-(x)\alpha_{\mathrm{Hh}} - \frac{\chi\,[\mathrm{Hh}]_{\mathrm{ss}}}{\beta_{\mathrm{Ptc}} + \gamma_{\mathrm{Hh\_Ptc}}[\mathrm{Hh}]_{\mathrm{ss}}}\left[S^+(x)\alpha_{ptc0} + \frac{\alpha_{ptc}[\mathrm{Hh}]_{\mathrm{ss}}^{nm}}{\eta\left[\kappa^n + [\mathrm{Hh}]_{\mathrm{ss}}^n\right]^m + [\mathrm{Hh}]_{\mathrm{ss}}^{nm}}\right] - \beta_{\mathrm{Hh}}[\mathrm{Hh}]_{\mathrm{ss}} = 0, \quad (S1)$$

with $\chi = \dfrac{T_{\mathrm{Ptc}}\gamma_{\mathrm{Hh\_Ptc}}}{\beta_{ptc}}$, $\kappa = \dfrac{k_{\mathrm{Signal}}\beta_{\mathrm{Hh\_Ptc}}}{\gamma_{\mathrm{Hh\_Ptc}}}$, and $\eta = \dfrac{k_{ptc}\beta_{\mathrm{Signal}}}{\alpha_{\mathrm{Signal}}}$, and satisfying the boundary

conditions $\dfrac{d[\mathrm{Hh}]_{\mathrm{ss}}}{dx}\bigg|_{x=-100} = \dfrac{d[\mathrm{Hh}]_{\mathrm{ss}}}{dx}\bigg|_{x=100} = 0.$

Equation (S1) is still difficult to solve analytically but can be used to compute steady-state profiles numerically. The solution of the full model [Equations (2.1)-(2.5)] approaches the steady-state solution of the last equation and is practically undistinguishable after 8 hours of simulation time (data not shown).

At the steady state, it is also possible to write each variable as an explicit function of $[\mathrm{Hh}]_{\mathrm{ss}}$. An example is the steady-state profile of $[\mathrm{Signal}]_{\mathrm{ss}}$ as a function of the extracellular gradient $[\mathrm{Hh}]_{\mathrm{ss}}$ [Equation (2.6)]. Figure 2.1E shows that based on the estimation of the parameter n (Fig. 2.1D and next section), the shape of the $[\mathrm{Signal}]_{\mathrm{ss}}$ profile is step-like. In this situation, the parameter ε defined in Equation (2.6) can be interpreted as a 'switching threshold' (see below for discussion of this concept). If a cell experiences an extracellular concentration of Hh higher than ε, Hh signaling will be

activated in that cell, while if $[Hh]_{ss} < \varepsilon$, then that cell will not be responsive to the Hh pathway. This binary behavior of the system is, of course, only strictly true when $n \to \infty$. In practice, this is only an approximation and therefore cells that experience extracellular Hh levels similar to ε will produce 'intermediate' levels of "Signal." Therefore, it is appropriate to ask what is the size of the region expressing these 'intermediate' levels of "Signal" at steady-state when $n > 6.8$. A simple inspection of Figure 2.1E suggests that $[Signal]_{ss}$ levels change from nearly maximal to nearly minimal within < 3 cell diameters. However, it is not clear what the range of $[Signal]_{ss}$ is that can activate Hh signalling *in vivo*. Morphogen studies in *Xenopus* suggest that 100 active receptors is about the lowest signaling concentration that cells can respond to [27]. If we consider similar numbers for the signal transducer pSmo in our system (which is also a transmembrane molecule), this is about 0.03 μM. In our simulation results of Figure 2.1E, a cell at position 9 would express already lower levels of [Signal] at the steady state. Thus, according to this analysis, we estimate that [Signal] levels drop from nearly maximal to undetectable in less 3 cells. Because this estimation depends on many uncertain parameters, we cannot strictly rule out that some concentration-dependent effects contribute to some extent to the final output. In fact, the small overlap between Col and dppZ detected in Figure 2.3F may be due to a slight concentration-dependent difference between the two target genes.

The steady-state interpretation of the Hh extracellular gradient in terms of Equation (2.6) requires some additional discussion. Since [Hh] refers to free unbound Hh concentration, strictly speaking, Equation (2.6) is not the relationship that describes how cells 'translate' extracellular levels into signaling outputs because cells probably do not

have another way of sensing extracellular Hh concentrations other than by using the receptor Ptc. This does not affect any of the predictions of the model. However, it is important to clarify the meaning of some parameters. For example, the interpretation of ε as the 'switching threshold' is somehow artificial, because cells (presumably) do not have a way to 'measure' unbound extracellular [Hh]. A more appropriate definition of 'switching threshold' may be obtained using an extracellular gradient that cells can sense. Since, all steady-state variables can be written as a function of $[Hh]_{ss}$, we can define more realistic 'switching thresholds.' For example, we can write $[Ptc]_{ss}$ as a function of $[Hh]_{ss}$ and set the switching threshold to be $[Ptc]_{ss}(\varepsilon)$. The switching threshold can also be defined in terms of $[Hh\_Ptc]_{ss}$, $\dfrac{[Hh\_Ptc]_{ss}}{[Ptc]_{ss}}$, or other combinations. Using the ratiometric model, the natural choice of switching threshold is given by

$$\delta = \frac{[Hh\_Ptc]_{ss}(\varepsilon)}{[Ptc]_{ss}(\varepsilon)} = \frac{\gamma_{Hh\_Ptc}}{\beta_{Hh\_Ptc}} \varepsilon = k_{Signal}. \qquad (S2)$$

Note that δ and ε are linearly proportional. Indeed, the last equation is just a particular case of a more general property of the system, namely, at steady-state, Equation (2.4) can be written in the form,

$$\frac{[Hh\_Ptc]_{ss}}{[Ptc]_{ss}} = \frac{\gamma_{Hh\_Ptc}}{\beta_{Hh\_Ptc}} [Hh]_{ss}. \qquad (S3)$$

Therefore, defining the switching threshold as ε or δ is equivalent. Nonetheless, δ (and not ε) is used as a 'switching threshold' in Figures 2.3 and 2.5. In any case, we insist that other choices do not affect the concept or the conclusions of this study.

Ratiometric model and estimation of n

Our mathematical analysis depends on the ratiometric model of Hh signaling interpretation [19]. Since this model has caused some controversy in the literature [28], it is appropriate to discuss possible problems that may arise in this treatment. The ratiometric interpretation of Hh signaling is a phenomenological model, this is, it is based on observations about target gene expression, but does not provide a molecular mechanism of Hh signal activation. In the past, it was thought that the levels of free (unliganded) Ptc would control the activity of the signal. In this scenario, signaling activity would not change as long as levels of free Ptc are maintained constant. The ratiometric model is introduced to explain the effect of [Hh_Ptc] levels in cells with a constant background of free Ptc [19]. To a first approximation, the ratiometric model explains how cells would correct the interpretation of a certain concentration of [Ptc] levels when also expressing [Hh_Ptc], but experiments in vertebrates or in different conditions suggest that the ratiometric model is probably not applicable in general. For example, the ratiometric model may be sensitive to total levels of Ptc, as experiments in vertebrates do not seem to obey the predictions of the model [29]. If so, the ratiometric model may not explain some mutants such as *ptc* overexpression. Despite these difficulties, the ratiometric model explains Hh patterning to a good approximation under normal physiological conditions. Because our analysis is based on the wild-type and many important details about Hh transduction are unknown, we argue that for the purpose of this study, the ratiometric model may be used as a phenomenological model of Hh signal interpretation.

An additional consideration is the use of the measurements from Casali and Struhl [19] to estimate the value of n. Here, we give a formal mathematical argument of the lower-bound estimation of n in Figure 2.1D. The basic idea is that n has a geometric meaning in the graph of the Hill function for which n is the Hill coefficient; it is a measure of the steepness of the Hill function. The following proposition shows that, given two points in the curve of the Hill function, it is possible to estimate a lower-bound estimate of n.

Proposition: Consider the function $F(x) = \dfrac{Ax^n}{k^n + x^n}$. Let x, y be real numbers and without loss of generality take $x \le y$. Then,

$$\frac{F(y) - F(x)}{y - x} \le F'(k) = \frac{An}{4k}$$

(If x=y, the left hand side is understood as the limit, i.e., $F'(x) \le F'(k)$).

Proof. By the intermediate value theorem of calculus, there is $x \le z \le y$ such that

$$\frac{F(y) - F(x)}{y - x} \le F'(z).$$

A simple computation shows that the maximum of F'(x) is reached when x=k. This completes the proof.

Let $F\left(\dfrac{\text{Hh\_Ptc}}{\text{Ptc}}\right) = \dfrac{100\% \left(\dfrac{[\text{Hh\_Ptc}]}{[\text{Ptc}]}\right)^n}{k^n_{\text{Signal}} + \left(\dfrac{[\text{Hh\_Ptc}]}{[\text{Ptc}]}\right)^n}$. The experiments of Casali and Struhl [19]

provide two data points in the graph of F as they made clones of *ptc⁻* cells in the anterior compartment expressing different amounts of the [Hh_Ptc]/[Ptc] ratio. For

$\dfrac{[\text{Hh\_Ptc}]}{[\text{Ptc}]} = 1.6$, they found no detectable activation of Hh target genes, and for

$\dfrac{[\text{Hh\_Ptc}]}{[\text{Ptc}]} = 2.7$, they found high expression of Hh outputs. We can, therefore, apply the

proposition above to obtain a lower-bound estimate of n. We assumed that F(1.6)=5%

and F(2.7)=95% to represent no and full activation of the pathway up to a 5% detection

error (95%). Unfortunately, Casali and Struhl did not compare gene expression levels in

the $\dfrac{[\text{Hh\_Ptc}]}{[\text{Ptc}]} = 2.7$ clone to wild-type gene expression in the same disc, but both Col and

a reporter of *dpp* appear strongly expressed in these clones [19]. Also, it is not clear

whether or not signaling activity is maximal for $\dfrac{[\text{Hh\_Ptc}]}{[\text{Ptc}]} = 2.7$, since Casali and Struhl

did not report whether or not *engrailed* was expressed in clones expressing this ratio.

Therefore, the accuracy of the estimate F(2.7) = 95% is unknown. However, reasonable

deviations of this choice do not affect our conclusions. For example, setting F(2.7) = 80%

gives the lower-bound estimate of n to be 5.7. As other caveats can be found in the use of

these data for the estimation of the value of n, we insist that to give an accurate and

reliable value of n is not a result or goal of this study. Instead, our estimation of n

suggests that the hypothesis that the steady-state [Signal] profile has a step-like shape is

reasonable and consistent with experimental findings.

Analysis of the Hh gradient in *ptc*-TPT and *ptc*+TPT discs

Hh signaling in *ptc*-TPT discs can be simulated using our mathematical model, with the

exception of Equation (2.2), which is replaced by

$$\frac{\partial[ptc]}{\partial t} = \alpha_{\text{TPT}} - \beta_{ptc}[ptc], \qquad\qquad (\text{S4})$$

and the initial condition (I.C.1) is replaced by $[ptc](x,0) = \dfrac{\alpha_{TPT}}{\beta_{ptc}}$. Compared to Equation

(2.2), the last equation eliminates all wild-type *ptc* expression and models ubiquitous

expression of *ptc* as introduced by the TPT transgene. Chen and Struhl estimated that two

copies of the TPT transgene introduce Ptc levels that are less than twofold compared to

the maximal levels of Ptc near the AP boundary [30]. Therefore, we set

$\alpha_{TPT} = \dfrac{\alpha_{ptc}}{5} \approx 5.4 \times 10^{-6}$ μM s^{-1} in the numerical simulations of Hh signaling in *ptc*-TPT

discs.

Regarding the levels introduced by the TPT transgene, it is important to clarify

that in a previous report it was observed that dppZ expands further anteriorly with respect

to the wild-type pattern (reported as data not shown in ref. [30]). However, in our own

experiments we observe that the dppZ domain is slightly reduced with respect to the wild

type (Fig. 2.3B,E). This apparent discrepancy may be due by one of the following

reasons. First, it is possible that the Chen and Struhl [30] used another insertion of the

TPT transgene, for example, one on the second chromosome. Or second, the TPT

transgene may have acquired mutations in the past decade that affected the performance

of the original transgene. In any case, the predictions of the Overshoot Model are not

affected by the strength of the transgene. The Overshoot Model predicts the Col and

dppZ patterns to overlap regardless of whether each pattern expands or reduces with

respect to the wild type.

Although the profiles shown in Figure 2.3G,H are intended as illustrations of the

predictions of the Classical Morphogen Model vs. Overshoot Model in different genetic

backgrounds, it is illustrative to estimate the expected size of the dppZ domain that would

not overlap with the Col pattern in *ptc*-TPT discs according to the interpretation of the Classical Morphogen Model. One way of doing this is to measure the size of the Col vs. dppZ domain in wild-type discs and use the numerical simulations to predict the expected non-overlapping region in *ptc*-TPT discs. However, this estimate will depend on the parameter values used in the simulations, as well as in our accuracy to measure the dppZ domain, which is difficult to estimate reliably because unlike Col, in wild-type discs the anterior boundary of the dppZ is not sharp (Fig. 2.3C).

Another way of estimating the difference in Col and dppZ patterns according to the Classical Morphogen model interpretation is to compare the shape of the Hh gradient in the region anterior to the Ptc/Col domain ($x > x_{ptc/col}$, with $x_{ptc/col}$ denoting the position of the anterior border of Ptc/Col, which we assume is the same throughout this analysis). As Ptc is not upregulated by Hh signaling in this region, we can assume that Ptc levels are approximately constant (denoted by $[Ptc]_A$) so that Equation (2.1) at steady-state is linear and given by

$$0 = D\frac{d^2[\text{Hh}]_{\text{SS}}}{dx^2} - \left(\gamma_{\text{Hh\_Ptc}}[\text{Ptc}]_A + \beta_{\text{Hh}}\right)[\text{Hh}]_{\text{SS}}, \qquad \text{(S5)}$$

subject to the boundary condition $[\text{Hh}]_{\text{SS}}(x_{\text{ptc}})=T_1$, which assumes that the Ptc boundary is set by a fixed concentration threshold, denoted by T_1. Equation (S5) has the following solution,

$$[\text{Hh}]_{\text{ss}}(x) = T_1 \exp\left[-\frac{x - x_{\text{ptc/col}}}{\lambda}\right] \qquad (x > x_{\text{ptc/col}}), \qquad \text{(S6)}$$

where $\lambda = \sqrt{\dfrac{D}{\gamma_{\text{Hh\_Ptc}}[\text{Ptc}]_A + \beta_{\text{Hh}}}}$ is the characteristic length of the gradient. In the context of the Classical Morphogen model, λ is actually a good representation of the width of the

non-overlapping domain. Equations (S5-S6) are also valid in *ptc*+TPT and *ptc*-TPT discs provided that the constant [Ptc]$_A$ is adjusted appropriately. Thus, we can compare what are the expected differences in the Col and dppZ domains in these backgrounds according to the Classical Morphogen model. If we denote [Ptc]$_0$ the anterior Ptc levels in wild-type discs, and assume that the levels of Ptc introduced by the TPT transgene can be denoted by [Ptc]$_{TPT}$ (from measurements of an earlier study using the TPT transgene, it can been estimated that [Ptc]$_{TPT}$/[Ptc]$_0$=1.4), then the predicted differences in Col/Ptc and dppZ domains in different mutant backgrounds are given by:

$$\lambda_{WT} = \sqrt{\frac{D}{\gamma_{Hh\_Ptc}[Ptc]_0 + \beta_{Hh}}} \qquad \text{(in wild-type discs)}$$

$$\lambda_{ptc\text{-}TPT} = \sqrt{\frac{D}{\gamma_{Hh\_Ptc}[Ptc]_{TPT} + \beta_{Hh}}} \qquad \text{(in } ptc\text{-TPT discs)} \qquad \text{(S7)}$$

$$\lambda_{ptc+TPT} = \sqrt{\frac{D}{\gamma_{Hh\_Ptc}([Ptc]_0 + [Ptc]_{TPT}) + \beta_{Hh}}} \qquad \text{(in } ptc\text{+TPT discs).}$$

Thus, Equations (S7) provide quantitative proof of our predictions in Figure 2.4A-C, namely, $\lambda_{ptc\text{-}TPT} > \lambda_{ptc+TPT}$ independently on the Ptc levels expressed by the TPT transgene. Our data in Figure 2.4F' show that experimentally $\lambda_{ptc+TPT}$ is at least 3 cells wide, suggesting that the non-overlapping region in *ptc*-TPT would be larger than 3 cells. This prediction is clearly not consistent with the observations in Figure 2.3F', demonstrating that the patterns in these mutant backgrounds cannot be explained by the Classical Morphogen model. Thus, this analysis provides strong support for the Overshoot model over the Classical Morphogen model in this system.

SUPPORTING REFERENCES

1. Lander AD (2007) Morpheus unbound: reimagining the morphogen gradient. Cell 128: 245-256.

2. Eldar A, Rosin D, Shilo BZ, Barkai N (2003) Self-enhanced ligand degradation underlies robustness of morphogen gradients. Dev Cell 5: 635-646.

3. Bollenbach T, Kruse K, Pantazis P, Gonzalez-Gaitan M, Julicher F (2005) Robust formation of morphogen gradients. Phys Rev Lett 94: 018103.

4. Gunbin KV, Omelyanchuk LV, Kogai VV, Fadeev SI, Kolchanov NA (2007) Model of the reception of hedgehog morphogen concentration gradient: comparison with an extended range of experimental data. J Bioinform Comput Biol 5: 491-506.

5. Nahmad M, Glass L, Abouheif E (2008) The dynamics of developmental system drift in the gene network underlying wing polyphenism in ants: a mathematical model. Evol Dev 10: 360-374.

6. Lander AD, Nie Q, Wan FY (2002) Do morphogen gradients arise by diffusion? Dev Cell 2: 785-796.

7. Garcia-Bellido A, Merriam JR (1971) Genetic Analysis of Cell Heredity in Imaginal Discs of Drosophila melanogaster. Proc Natl Acad Sci U S A 68: 2222-2226.

8. Held LI (2002) Imaginal discs : the genetic and cellular logic of pattern formation. Cambridge [England]; New York: Cambridge University Press. xv, 460 p. p.

9. Bollenbach T, Pantazis P, Kicheva A, Bokel C, Gonzalez-Gaitan M, et al. (2008) Precision of the Dpp gradient. Development 135: 1137-1146.

10. Gonzalez-Gaitan M, Capdevila MP, Garcia-Bellido A (1994) Cell proliferation patterns in the wing imaginal disc of Drosophila. Mech Dev 46: 183-200.

11. Teleman AA, Cohen SM (2000) Dpp gradient formation in the Drosophila wing imaginal disc. Cell 103: 971-980.

12. Kicheva A, Pantazis P, Bollenbach T, Kalaidzidis Y, Bittig T, et al. (2007) Kinetics of morphogen gradient formation. Science 315: 521-525.

13. Hufnagel L, Teleman AA, Rouault H, Cohen SM, Shraiman BI (2007) On the mechanism of wing size determination in fly development. Proc Natl Acad Sci U S A 104: 3835-3840.

14. Han C, Belenkaya TY, Wang B, Lin X (2004) Drosophila glypicans control the cell-to-cell movement of Hedgehog by a dynamin-independent process. Development 131: 601-611.

15. Panakova D, Sprong H, Marois E, Thiele C, Eaton S (2005) Lipoprotein particles are required for Hedgehog and Wingless signalling. Nature 435: 58-65.

16. Torroja C, Gorfinkiel N, Guerrero I (2004) Patched controls the Hedgehog gradient by endocytosis in a dynamin-dependent manner, but this internalization does not play a major role in signal transduction. Development 131: 2395-2408.

17. Su VF, Jones KA, Brodsky M, The I (2007) Quantitative analysis of Hedgehog gradient formation using an inducible expression system. BMC Dev Biol 7: 43.

18. von Dassow G, Meir E, Munro EM, Odell GM (2000) The segment polarity network is a robust developmental module. Nature 406: 188-192.

19. Casali A, Struhl G (2004) Reading the Hedgehog morphogen gradient by measuring the ratio of bound to unbound Patched protein. Nature 431: 76-80.

20. Strigini M, Cohen SM (1997) A Hedgehog activity gradient contributes to AP axial patterning of the Drosophila wing. Development 124: 4697-4705.

21. Kicheva A, Gonzalez-Gaitan M (2008) The Decapentaplegic morphogen gradient: a precise definition. Curr Opin Cell Biol 20: 137-143.

22. Gurdon JB (1974) The control of gene expression in animal development. Cambidge, Mass.: Harvard University Press.

23. Lodish HF (1976) Translational control of protein synthesis. Annu Rev Biochem 45: 39-72.

24. Gaskill P, Kabat D (1971) Unexpectedly large size of globin messenger ribonucleic acid. Proc Natl Acad Sci U S A 68: 72-75.

25. Gallet A, Therond PP (2005) Temporal modulation of the Hedgehog morphogen gradient by a patched-dependent targeting to lysosomal compartment. Dev Biol 277: 51-62.

26. Denef N, Neubuser D, Perez L, Cohen SM (2000) Hedgehog induces opposite changes in turnover and subcellular localization of patched and smoothened. Cell 102: 521-531.

27. Dyson S, Gurdon JB (1998) The interpretation of position in a morphogen gradient as revealed by occupancy of activin receptors. Cell 93: 557-568.

28. Zhu AJ, Scott MP (2004) Incredible journey: how do developmental signals travel through tissue? Genes Dev 18: 2985-2997.

29. Taipale J, Cooper MK, Maiti T, Beachy PA (2002) Patched acts catalytically to suppress the activity of Smoothened. Nature 418: 892-897.

30. Chen Y, Struhl G (1996) Dual roles for patched in sequestering and transducing Hedgehog. Cell 87: 553-563.

Supporting Protocol

The following protocol explains how the expression of Ptc was quantified to generate the concentration profiles in Fig. 2.2E. This process was followed with each image manually one at a time. The process was repeated independently twice in each image and the final result was averaged. For each time point, 4-7 discs were analyzed.

1. The original image was passed through a Gaussian filter (medfilt2 in Matlab).

2. Crop a 30X30 pixel box manually from the Posterior compartment of the filtered image and compute the average pixel intensity. This is the background intensity.

3. Subtract the background intensity to the whole filtered image.

4. Crop a 30X30 pixel box manually from the Anterior compartment (far from the AP boundary) of the filtered-background subtracted image and compute the average pixel intensity. This is the "Ptc basal intensity".

5. Crop a 20X80 pixel box that crosses the AP boundary in a place that the posterior border of Ptc looks approximately straight (as the red box in the cartoon of Figure 2.2E). Average the intensities of each of the 20 lines that are perpendicular to the AP boundary.

6. Divide the average intensity at each point by the "Ptc basal intensity". This gives the intensity profiles in units of the "Ptc basal intensity". In Figure 2E, all profiles were plotted on the same relative scale.

7. Finally, the width in Figure 2.2F is defined as the distance between the points that cross an intensity equal to 2 (this is twice the Ptc basal levels). Widths for the same time points were averaged along their standard deviation and are plotted in Figure 2.2F.

**Supporting Table 2.1**. Wild-type parameter values used in the numerical simulations.

Parameter	Description	Value
D	Hh diffusion coefficient	$0.5\ \mu m^2 s^{-1}$
α_{Hh}	Hh maximal activation rate	$3.4 \times 10^{-3}\ \mu Ms^{-1}$
α_{ptc}	*ptc* maximal activation rate	$2.7 \times 10^{-5}\ \mu Ms^{-1}$
α_{ptc0}	*ptc* basal transcription rate	$3.8 \times 10^{-6}\ \mu Ms^{-1}$
α_{Signal}	Signal maximal activation rate	$1.6 \times 10^{-4}\ \mu Ms^{-1}$
β_{Hh}	Hh degradation rate	$3.3 \times 10^{-3}\ s^{-1}$
β_{ptc}	*ptc* degradation rate	$1.4 \times 10^{-4}\ s^{-1}$
β_{Ptc}	Ptc degradation rate	$1.5 \times 10^{-3}\ s^{-1}$
β_{Signal}	'Signal' degradation rate	$5.5 \times 10^{-4}\ s^{-1}$
β_{Hh_Ptc}	Hh_Ptc degradation rate	$1.5 \times 10^{-3}\ s^{-1}$
γ_{Hh_Ptc}	Association rate, Hh_Ptc complex	$7.15 \times 10^{-2}\ \mu M^{-1}s^{-1}$
T_{Ptc}	Ptc translation rate	$3.6 \times 10^{-3}\ s^{-1}$
k_{ptc}	*ptc* half-maximal activation conc.	$0.14\ \mu M$
k_{Signal}	[Signal] half-maximal activation	2.135
m	Hill coefficient (*ptc* activation)	3
n	Hill coefficient ('Signal' activation)	6.8

(Parameter values are estimated from previous theoretical and experimental studies; see

Nahmad and Stathopoulos (2009) for details).
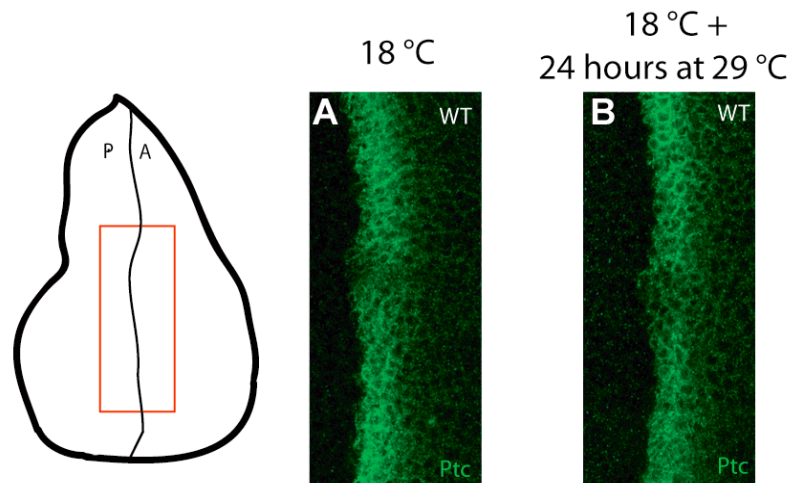
Supporting Fig. 2.1 Temperature changes do not affect Ptc expression.

Wild-type discs from larvae raised at 18°C (A) or from larvae raised at 18°C followed by

24 h at 29°C (B) immunolabeled for Ptc. Fixation, immunostaining, and imaging of discs

in (A and B) were performed under identical conditions.
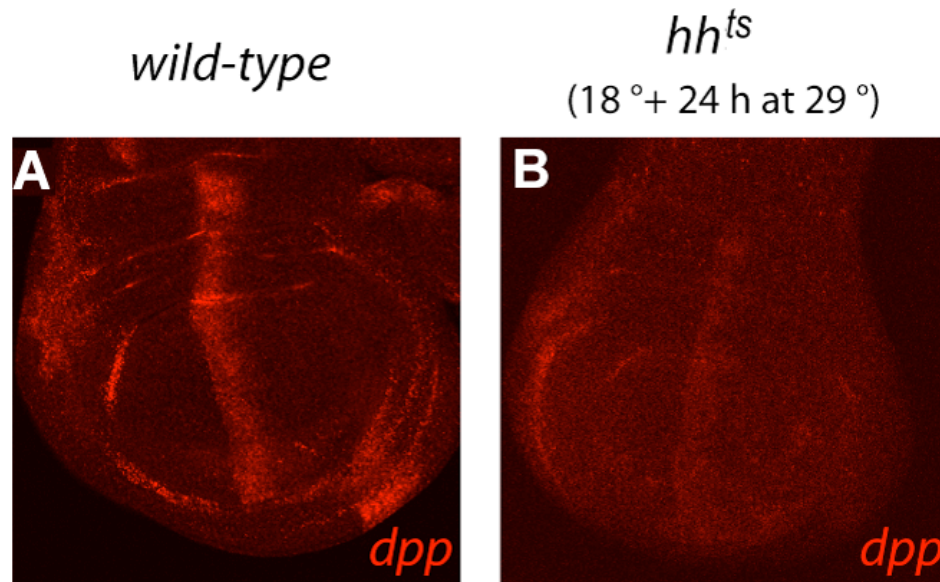
**Supporting Fig. 2.2 dpp expression is maintained after Hh signaling is interrupted.**
In situ hybridization using a riboprobe to dpp in a wild-type disc (A) versus a hhts2
homozygous disc (B) grown at 18°C and exposed to 29°C for the last 24 h of the third
larval instar. The domain of dpp expression is similar in (A and B), but the intensity of
expression is higher in wild type. If residual Hh levels were to account for this
expression, then dpp expression domain would be predicted to shift in expression toward
the AP boundary; the full extent of the pattern would not be expected.
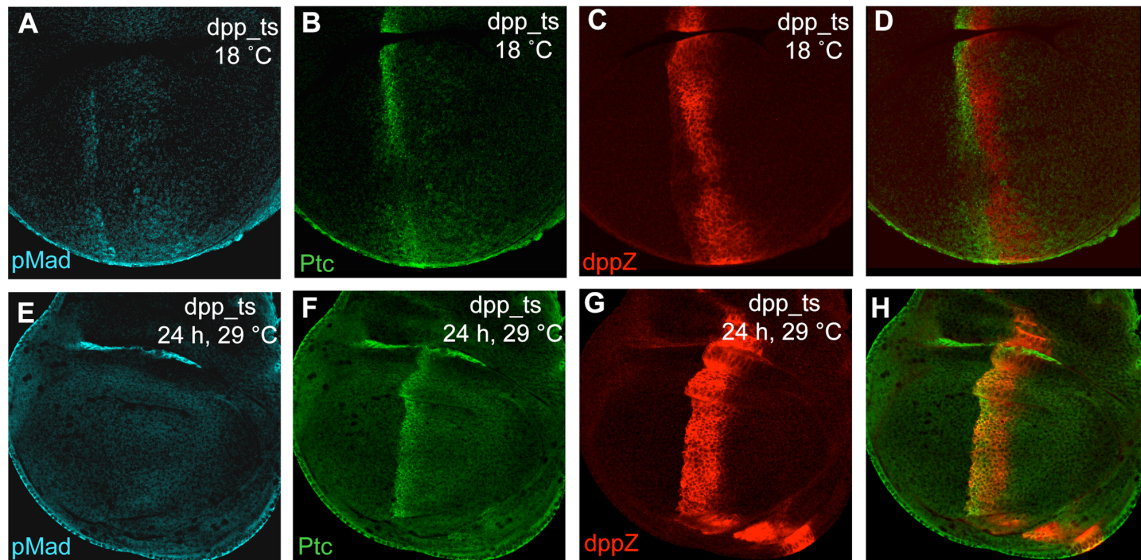
**Supporting Fig. 2.3 dppZ and Ptc expression patterns are normal after Dpp signaling interruption.**

(A–C) dpp^{hr56}/dpp^{hr4} animals raised at 18°C are normal in Dpp signal transduction assayed by pMAD expression (A) and have normal patterns of Ptc (B) and dppZ (C). (D) Merge of the patterns displayed in (B and C). (E–G) dpp^{hr56}/dpp^{hr4} larvae exposed to restrictive temperature (29°C) for 24 h have lost their pMAD expression pattern (E), and yet, Ptc and dppZ are approximately normal (F and G). The patterns do not overlap, suggesting that Dpp signaling is not required for maintenance of *dpp* expression in the nonoverlapping region. (H) Merge of the patterns displayed in (F and G). In this figure, the dppZ transgene is an insertion on chromosome III, to allow assay in a dpp mutant background.
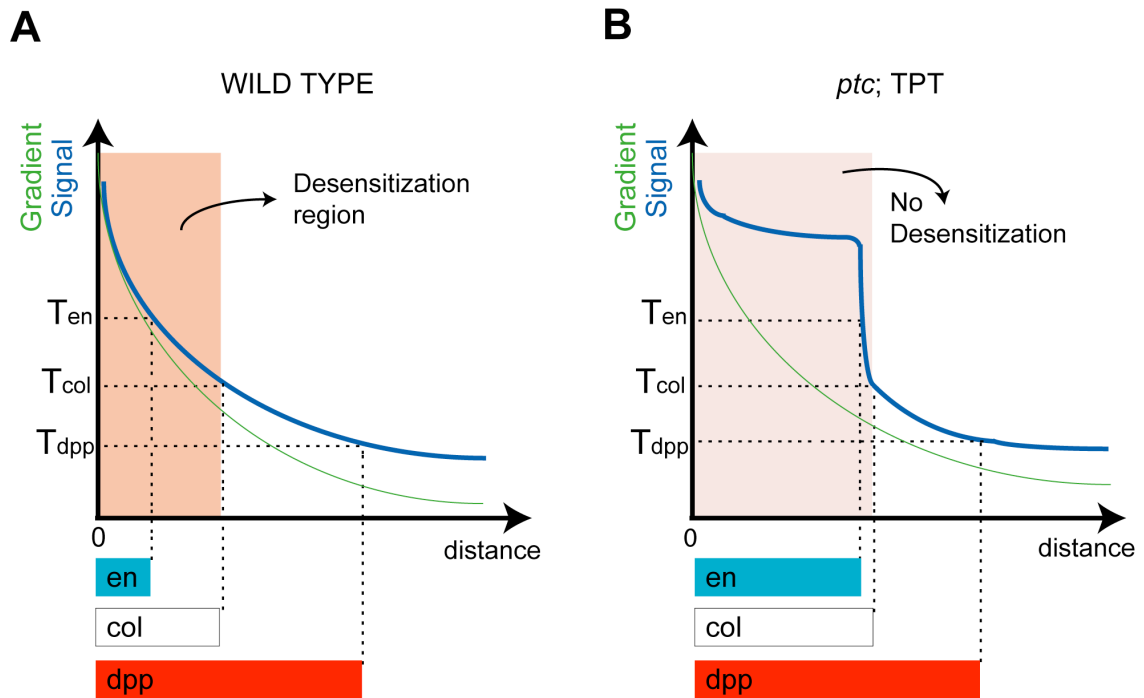
Supporting Fig. 2.4 The overlap of Col and dppZ in *ptc*−TPT discs cannot be explained by the Temporal Adaptation model.

Predictions of Hh patterning in wild-type (A) versus *ptc*−TPT discs (B) according to the Temporal Adaptation model (Dessaud et al., 2007). In wild-type discs (A), Ptc-mediated desensitization is required to map different concentrations of the extracellular gradient (green) into a graded signal response (blue). However, when signal-mediated Ptc up-regulation is impaired, cells are unable to differentially "desensitize" the levels of the signal and respond similarly to different concentrations of the signaling (B). Thus, lack of desensitization in ptc−TPT discs results in the expansion of the highest response (e.g., en; blue) to the extent of the intermediate response (e.g., col; white), but should have little or no effect in the differential establishment of the dppZ and Col borders, because Ptc-mediated desensitization is a cell-autonomous effect.
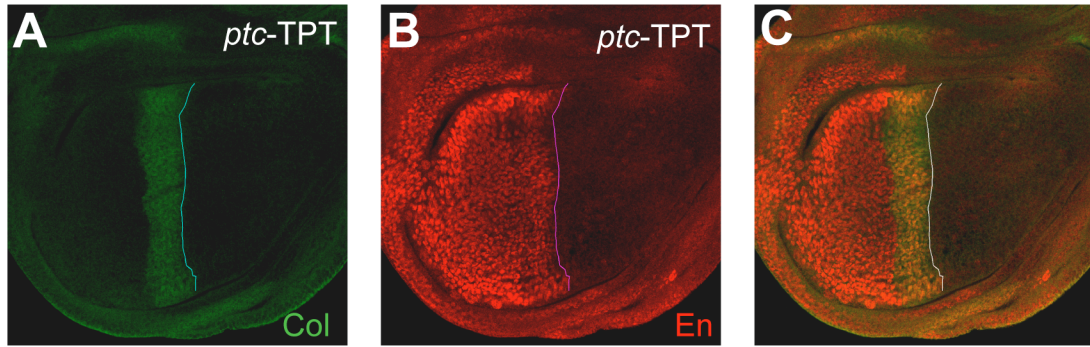
Supporting Fig. 2.5 Col and the anterior pattern of En overlap in *ptc*−TPT discs. Col (A) and En (B) are expressed in nearly the same domain in the anterior compartment in late third instar *ptc*−TPT discs. (C) Merge of panels displayed in (A and B). The line drawn from the Col pattern shows that Col and En approximately share their anterior border.
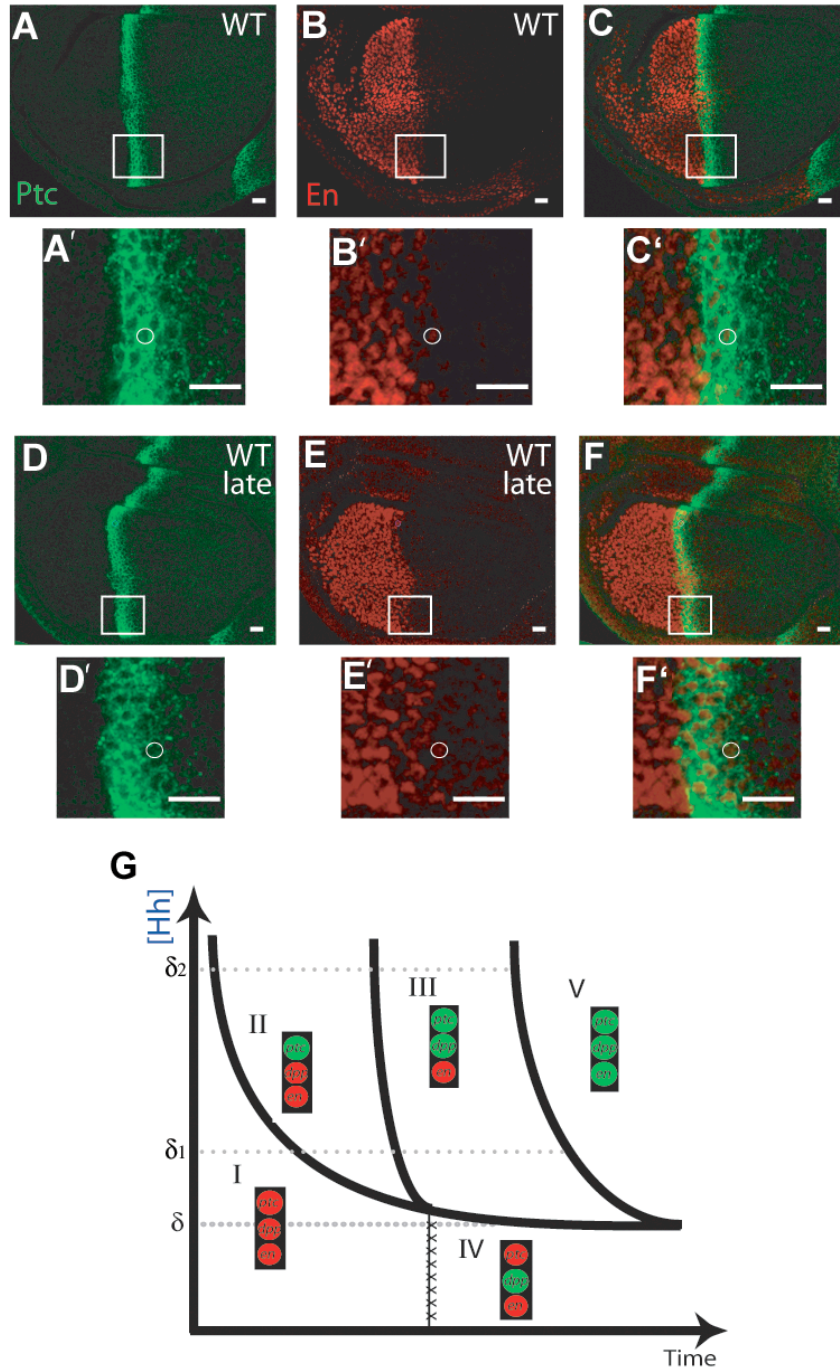
Supporting Fig. 2.6 Hh-dependent expression of Ptc and En approximately overlap in late wild-type discs.

(A and B) Immunostaining of wild-type wing discs from a crawling third instar larva using anti-En (A) and anti-Ptc (B) antibodies. (C) Merge of images in (A and B). (A′–C′)

4× magnification of the white box depicted in (A–C). White circles mark a cell in the anterior border of the En pattern showing that at this time, the En border approximately falls within the domain of Ptc expression, but does not share the same anterior boundary. (D and E) Same as (A and B), but from a third larva close to pupariation. (F) Merge of images in (D and E). (D′–F′) Magnification of the white box in (D–F). Scale bars indicate 10 μm. White circles mark a cell at the anterior boundary of the En pattern, showing that at this time, the En and Ptc anterior borders coincide. (G) Generalization of the state-space model in Figure 2.5 to incorporate *engrailed*. No additional concentration threshold is required to define the en domain of expression. Instead, en seems to be responsive to integration of Hh signaling over time, as it shares an anterior boundary with Ptc, and presumably Col, at later time points. Therefore, cells exposed to two different Hedgehog concentrations $\delta 1$ and $\delta 2$ above the switching threshold, δ, turn on Hh target gene expression at different time points but eventually activate all target genes (Territory V).

Supporting Materials for Chapter 3

Supporting Text

Linear approximation of the Hh steady-state gradient

Consider the model of Hh signaling in the *Drosophila* wing disc [Equations (3.5)]. At steady-state, simple algebraic substitutions reduce the system of equations to a single piecewise ordinary differential equation,

$$D\frac{d^2[\text{Hh}]_{ss}}{dx^2} + S^-(x)\alpha_{\text{Hh}} - \frac{S^+(x)\chi\,[\text{Hh}]_{ss}}{\beta_{\text{Ptc}} + \gamma_{\text{Hh\_Ptc}}[\text{Hh}]_{ss}}\left[\alpha_{ptc0} + \frac{\alpha_{ptc}[\text{Hh}]_{ss}^{nm}}{k_{ptc}\beta_{\text{Signal}}\left[\kappa^n + [\text{Hh}]_{ss}^n\right]^m + \alpha_{\text{Signal}}[\text{Hh}]_{ss}^{nm}}\right] - \beta_{\text{Hh}}[\text{Hh}]_{ss} = 0 \quad (A1)$$

with $\chi = \dfrac{T_{\text{Ptc}}\gamma_{\text{Hh\_Ptc}}}{\beta_{ptc}}$ and $\kappa = \dfrac{k_{\text{Signal}}\beta_{\text{Hh\_Ptc}}}{\gamma_{\text{Hh\_Ptc}}}$. In the anterior compartment, $S^-(x) = 0$ and

$S^+(x) = 1$, and Equation (A1) reduces to Equation (3.6) which can be linearised to obtain an approximate solution for the Hh steady-state gradient near the AP boundary [Equation (3.8)]. Here, we provide the details of this linearization that were omitted in the text. Near the AP boundary, Hh is present at sufficiently high levels that we can assume $[\text{Hh}]_{SS}^n \gg \kappa^n$ (see below) so that the following approximation holds,

$$\frac{\alpha_{ptc}[\text{Hh}]_{ss}^{nm}}{\eta\left[\kappa^n + [\text{Hh}]_{ss}^n\right]^m + [\text{Hh}]_{ss}^{nm}} \approx \frac{\alpha_{ptc}}{\eta+1}.$$

This expression reduces one nonlinear term in Equation (3.6) to a constant. The other nonlinear term can be approximated by a linear function near a point of interest $\left([\text{Hh}]_{SS}^0\right)$ via a Taylor expansion:

$$f\left([\text{Hh}]_{\text{SS}}\right) = \frac{\chi\,[\text{Hh}]_{\text{ss}}}{\beta_{\text{Ptc}} + \gamma_{\text{Hh\_Ptc}}[\text{Hh}]_{\text{ss}}} \approx f\left([\text{Hh}]_{\text{SS}}^{0}\right) + \frac{df}{d[\text{Hh}]_{\text{ss}}}\left([\text{Hh}]_{\text{SS}}^{0}\right)\left([\text{Hh}]_{\text{ss}} - [\text{Hh}]_{\text{SS}}^{0}\right)$$

$$\approx \frac{\chi}{\beta_{\text{Ptc}} + \gamma_{\text{Hh\_Ptc}}[\text{Hh}]_{\text{SS}}^{0}}\left[\frac{\gamma_{\text{Hh\_Ptc}}[\text{Hh}]_{\text{SS}}^{0\ 2}}{\beta_{\text{Ptc}} + \gamma_{\text{Hh\_Ptc}}[\text{Hh}]_{\text{SS}}^{0}} + \left(1 - \frac{\gamma_{\text{Hh\_Ptc}}[\text{Hh}]_{\text{SS}}^{0}}{\beta_{\text{Ptc}} + \gamma_{\text{Hh\_Ptc}}[\text{Hh}]_{\text{SS}}^{0}}\right)[\text{Hh}]_{\text{ss}}\right].$$

The maximum $[\text{Hh}]_{\text{SS}}$ levels are limited by the ratio of the Hh production rate (α_{Hh}) to the Hh degradation rate (β_{Hh}) and numerical estimates suggest that $[\text{Hh}]_{\text{SS}}$ rapidly drops to one third of this maximal value within a few cells diameters from the AP boundary (Fig. 3.3B). Therefore, substituting $[\text{Hh}]_{\text{SS}}^{0} = \frac{1}{3}\frac{\alpha_{\text{Hh}}}{\beta_{\text{Hh}}}$ (which also satisfies the condition of the previous approximation: $\left[\frac{1}{3}\frac{\alpha_{\text{Hh}}}{\beta_{\text{Hh}}}\right]^{n} >> \kappa^{n}$ using the parameter values in Supporting Table 2.1) in the Taylor expansion above we get,

$$\frac{\chi\,[\text{Hh}]_{\text{ss}}}{\beta_{\text{Ptc}} + \gamma_{\text{Hh\_Ptc}}[\text{Hh}]_{\text{ss}}} \approx \frac{3\chi\beta_{\text{Hh}}}{3\beta_{\text{Hh}}\beta_{\text{Ptc}} + \alpha_{\text{Hh}}\gamma_{\text{Hh\_Ptc}}}\left[\frac{\gamma_{\text{Hh\_Ptc}}\alpha_{\text{Hh}}^{2}}{9\beta_{\text{Hh}}^{2}\beta_{\text{Ptc}} + 3\alpha_{\text{Hh}}\beta_{\text{Hh}}\gamma_{\text{Hh\_Ptc}}} + \left(1 - \frac{\alpha_{\text{Hh}}\gamma_{\text{Hh\_Ptc}}}{3\beta_{\text{Hh}}\beta_{\text{Ptc}} + \alpha_{\text{Hh}}\gamma_{\text{Hh\_Ptc}}}\right)[\text{Hh}]_{\text{ss}}\right].$$

These approximations turn Equation (3.6) into a linear equation [Equation (3.7)] which can be solved analytically once boundary conditions are provided. The boundary condition at the anterior end is completely irrelevant and can be ignored (i.e. assumed at infinity) because the range of the $[\text{Hh}]_{\text{SS}}$ gradient is much shorter than the width of the anterior compartment. However, the solution [Equation (3.8)] is only fully determined once the boundary conditions at $x=0$ are specified. In fact, the parameter A in Equation (3.8) is determined by imposing continuity of the gradient (and its derivative) at the AP boundary. Note that Equation (A1) in the posterior compartment takes the following simple form:

$$D\frac{d^{2}[\text{Hh}]_{\text{ss}}}{dx^{2}} + \alpha_{\text{Hh}} - \beta_{\text{Hh}}[\text{Hh}]_{\text{ss}} = 0.$$

Imposing a zero-flux boundary condition in the posterior end: $\left[\dfrac{d[\text{Hh}]_{\text{SS}}}{dx}\left(x=-L_{\text{P}}\right)=0\right]$,

the solution of this equation is:

$$[\text{Hh}]_{\text{SS}}(x)=\frac{\alpha_{\text{Hh}}}{\beta_{\text{Hh}}}-\text{M}\cosh\left[\frac{x+L_{\text{P}}}{\sqrt{D/\beta_{\text{Hh}}}}\right]\quad(\text{for } x\le 0),\qquad(\text{A2})$$

with M determined by boundary conditions at $x=0$. By continuity, Equations (3.8) and (A2) and their derivatives must coincide at $x=0$. This condition determines A (in Equation (3.8)) and M (in Equation (A2)) uniquely from a system of two algebraic equations:

$$\text{A}-\frac{\text{C}}{\text{B}}=\frac{\alpha_{\text{Hh}}}{\beta_{\text{Hh}}}-\text{M}\cosh\left[\sqrt{\frac{\beta_{\text{Hh}}}{D}}L_{\text{P}}\right]$$

$$\text{A}\sqrt{\text{B}}=\text{M}\sqrt{\frac{\beta_{\text{Hh}}}{D}}\sinh\left[\sqrt{\frac{\beta_{\text{Hh}}}{D}}L_{\text{P}}\right].$$

And simple algebraic substitutions give,

$$\text{A}=\frac{\dfrac{\alpha_{\text{Hh}}}{\beta_{\text{Hh}}}+\dfrac{\text{C}}{\text{B}}}{1+\sqrt{\dfrac{\text{B}D}{\beta_{\text{Hh}}}}\coth\left(\sqrt{\dfrac{\beta_{\text{Hh}}}{D}}L_{\text{P}}\right)}.$$

This analysis permits to obtain a linear approximation of the Hh gradient near the AP boundary and defines the approximate steady-state invariant set described by Equations (3.9).

Geometric Properties of Steady-State Invariant Sets

Given the practical purposes of the study, we considered steady-state invariant perturbations as a subset of parameter space, but their geometric properties were not

stated in detail. Here, we briefly discuss some general geometrical properties of steady-state invariant sets and discuss potential advantages of a geometric treatment. Steady-state invariant sets are defined by systems of algebraic equations (in many cases by polynomial equations), and therefore, they are real semi-algebraic varieties. As such, geometric properties such as their dimension (or codimension) are well defined. Although a formal treatment of the geometry of steady-state invariant sets is beyond the scope of this study, it is important to realize that there is a vast literature of algebraic and geometric tools to analyze the properties steady-state invariant sets. Future geometric studies may provide insights into practical aspects of steady-state invariant sets. For example, how to decompose steady-state invariant sets into more simple varieties; and the existence of steady-state invariant subsets of codimension zero.
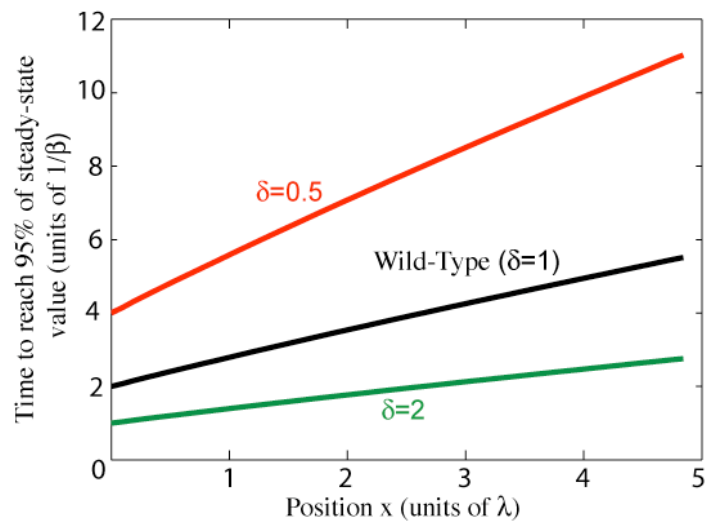
**Supporting Fig. 3.1**. **The time to reach the steady state is position-dependent.**

In the model of the single morphogen described by Equation (3.1), the time to reach the steady state is position-dependent. Cells located closer to the morphogen source approach the equilibrium faster than cells farther away from it. The same trend is observed for parameter perturbations along the steady-state invariant set (δ=0.5, red line; δ=2, green line). As a consequence of this spatial effect, cells sufficiently far from the source may not reach the equilibrium within the developmental timescale.
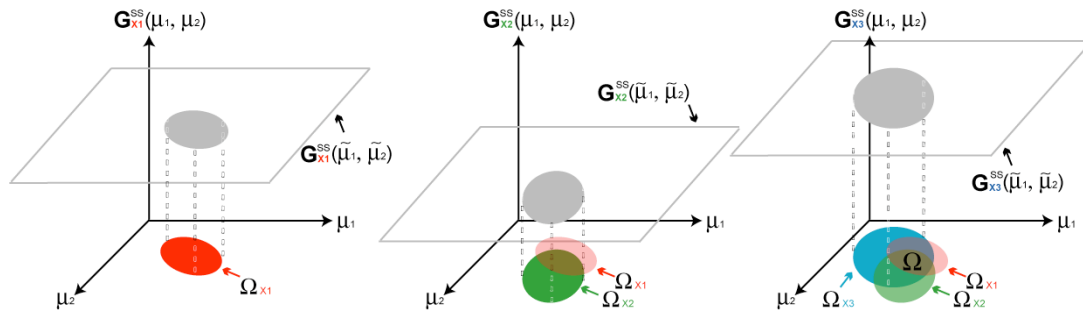
**Supporting Fig. 3.2. Geometric visualization of a general steady-state invariant set.** For a fixed spatial position, we can obtain the set of parameter values that leave the steady-state solution $\mathbf{G}^{SS}$ unchanged with respect to the wild-type (Equation (B4) in Box 3.1), i.e., the set of points in parameter space that are mapped into the same value of $\mathbf{G}^{SS}$ than the wild-type values. The figure shows a cartoon of these sets for three different points (denoted by Ω_{X1}, Ω_{X2}, and Ω_{X3}). The steady-state invariant set $\boldsymbol{\Omega}$ (in $\mathbf{S}=\{X1, X2, X3\}$) is given by the intersection of those sets (Equation (B5) in Box 3.1).

Supporting Materials for Chapter 4
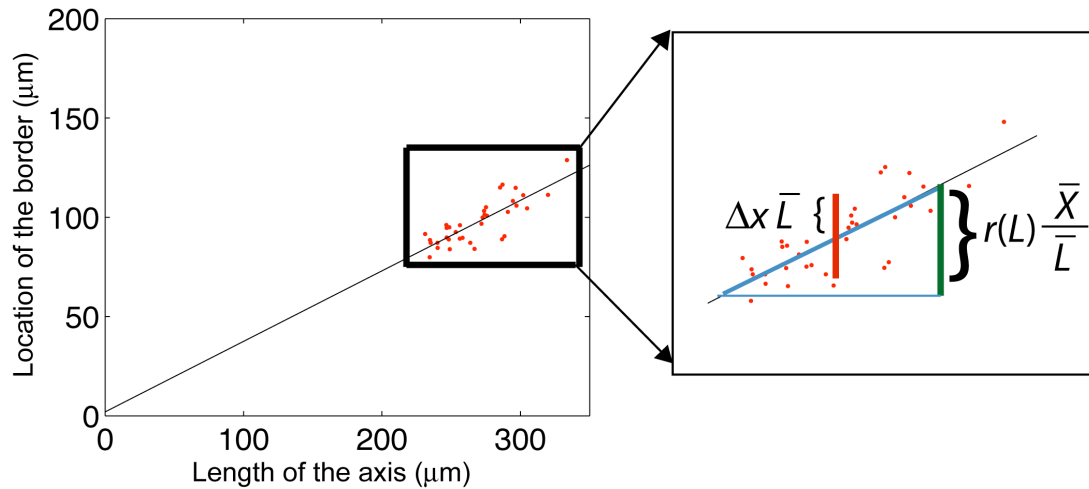
Supporting Fig. 4.1 Derivation of the scaling percentage level.

Given a plot of positional data vs. length of the domain, we can derive the scaling percentage level formula by comparing the variability in the positional data (red bar) to the height of a right triangle (green bar) of base equal to r(L) and slope defined by the ratio of the mean location to the mean axis length. The ratio of the red to green bars represents how much of the data can be explained by chance due to fluctuations in the X_i's. Thus, C is the percentage of scaling data that cannot be explained by variability on the positional data.
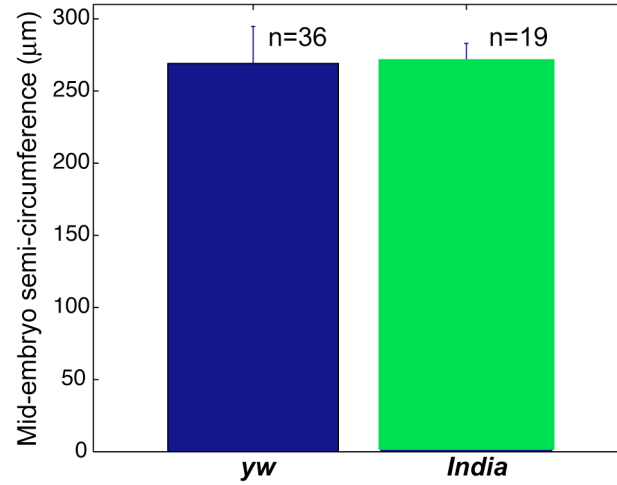
Supporting Fig. 4.2 *yw* **and India embryos do not display significant differences in the length of the DV axis.**

Although India and *w1118* embryos display significant differences along the AP axis

(Lott et al., 2007), measurements from cross sections show that they do not differ

significantly in the length of their DV axis.